Astronomy & Astrophysics manuscript no. output
May 9, 2026

Effect of impactor oblateness on the formation of lunar simple craters

Yichen Wang[1], Zhiyong Xiao[1,2,⋆], Rui Xu[1], Kai Wünnemann[3,4], and Jian-Yang Li[1]

[1] Planetary Environmental and Astrobiological Research Laboratory, School of Atmospheric Sciences, Sun Yat-sen University, Zhuhai, China
[2] State Key Laboratory of Lunar and Planetary Sciences, Macau University of Science and Technology, Taipa, Macau, China
[3] Museum für Naturkunde, Leibniz Institute for Evolution and Biodiversity Science, Berlin, Germany
[4] Institute of Geological Sciences, Freie Universität Berlin, Berlin, Germany

May 9, 2026

ABSTRACT

Context. Simple craters are ubiquitous on the Moon and are mainly formed by impactors of <1 km in diameter. Prevailing knowledge suggested that gravity-dominated simple craters follow uniform morphometric scaling, which is routinely employed to probe lunar subsurface structures and compositions. However, recent observations revealed that the morphometry of some pristine simple craters on the Moon deviate from the empirical scaling. The empirical morphometric scaling was largely established from impact experiments using spherical impactors, whereas small impactors to the Moon such as near-Earth objects (NEOs) are typically of irregular or ellipsoidal shapes. The effect of impactor oblateness on the formation of lunar simple craters remains unexplored.
Aims. We aim to investigate the effect of impactor oblateness on crater formation and their implications for the Moon and NEOs.
Methods. We used numerical modelling to study the effect of impactor oblateness (i.e., aspect ratios of 1:10 to 10:1) on crater formation.
Results. For impactors with identical kinetic energy, larger oblateness yields smaller and shallower craters, but critical morphometric parameters remain unaffected, suggesting that simple crater morphology is not diagnostic evidence of impactor shape. Impactor oblateness affects the sizes of shocked zones that experienced peak pressures lower than a given value, yielding two-orders-of-magnitude variations in impact melt volumes for different impactor oblateness. Oblate impactors generate rarefaction waves earlier than spherical impactors, accelerating shock energy dissipation beyond the melt zone and reducing the maximum excavation depth and cratering efficiency by up to 22% and 80%, respectively.
Conclusions. Empirical scaling relationships between the maximum excavation depth and crater geometries remain robust, verifying the reliability of using lunar simple craters as probes for subsurface structures and ejecta provenances. Considering the generally non-spherical shapes of NEOs with diameters of tens to hundreds of meters, their size distribution estimated using lunar simple crater diameters should have a revised power-law slope of -2.7, which is ~3.8% steeper than prior estimations.

Key words. Moon, Planets and satellites: surfaces, Planets and satellites: individual: Impact craters, Minor planets, asteroids: general

1. Introduction

Collisions by cosmic materials on the Moon form impact craters, among which simple craters are the smallest and most abundant morphological class (Melosh 1989). As implied by the name, simple craters have much simpler and more uniform morphology compared to larger complex craters and impact basins, as they typically exhibit a bowl shape and smooth crater walls (Shoemaker 1960). Formed by impactors smaller than about 1 km in diameter, simple craters with different diameters have long been regarded to have similar formation processes, as verified by physical simulations of spherical projectiles impacting flat and homogeneous targets (Gault et al. 1968; Holsapple & Schmidt 1987). Measurements of crater geometries further showed that for relatively large simple craters on the Moon whose formation processes are not significantly affected by target strengths, they have relatively uniform morphometric parameters (Pike 1974, 1980). For example, for fresh lunar simple craters that have rim-to-rim diameters (D) larger than ~400 m, their rim-to-floor depths (d) and rim heights (h) are ~0.2 and 0.04 of D, respectively (Pike 1974, 1977), and rim deposits originate from the maximum excavation depths that are ~0.1D (Croft 1980). The empirical morphometric parameters of lunar simple craters are largely verified by recent observations using high-resolution remote sensing data, especially for those with $D > 4$ km (Stopar et al. 2017; Krüger et al. 2018). Abnormally shallow craters are consistent with being secondary craters (i.e., secondaries) formed by lower velocity collisions of impact ejecta (Luo et al. 2025). The empirical assumption that newly formed simple craters on the Moon exhibit uniform morphometric characteristics has been widely used as a proxy of lunar subsurface structure and composition, including regolith thickness estimation (e.g., Oberbeck & Quaide 1968; Wilcox et al. 2005), stratigraphy reconstruction (e.g., Ma et al. 2025), and lunar sample provenance (e.g., Xie et al. 2020). However, recent observations reported that some pristine simple craters on the Moon with $D \approx 400$–4000 m have $d/D = 0.16$–0.25 (Stopar et al. 2017; Krüger et al. 2018; Wu et al. 2022), which were assumed to be formed in the gravity-dominated cratering regime (i.e., crater formation not significantly affected by target properties). The origin of this morphometric variability is understudied, casting

⋆ Corresponding author: xiaozhiyong@mail.sysu.edu.cn

Article published by EDP Sciences, to be cited as https://doi.org/10.1051/0004-6361/202659315

doubt on the reliability of using simple crater morphometry as a subsurface probe.

When studying the cratering mechanism of lunar simple craters, the effect of impactor shapes is frequently neglected, as typical hypervelocity impacts on planetary surfaces are well approximated by spherical projectiles whose initial kinetic energy is released similarly to that of point-source explosion (Holsapple & Schmidt 1987). However, small impactors to the Moon usually have irregular shapes (Holsapple 2001; Scheeres et al. 2015). For example, characterised by the ratio of the longest to shortest axis (i.e., aspect ratio or oblateness), rubble-pile asteroids typically have aspect ratios of less than 2:1–3:1 (Hatch & Wiegert 2015; Sugiura et al. 2018). Low-spin and high-cohesion asteroids reach theoretical aspect ratios of approximately 5:1–6:1 (Holsapple 2001), such as monolithic fragments ejected form planetary impacts that typically have high velocities and significant cohesive strength (Krishna & Kumar 2016). Rare potential impactors such as the highly flattened 'Oumuamua have larger aspect ratios of up to 10:1 ('Oumuamua ISSI Team et al. 2019). On the other hand, physical modelling of impact cratering showed that long rod-shaped or tapered projectiles yield deeper but smaller craters (e.g., Itagaki et al. 2019; Owen et al. 2022). The generally shallower floors of secondary craters are consistent with formation via clusters of impact ejecta rather than a single ejecta fragment (Schultz & Gault 1985; Xiao 2016). In addition, numerical and physical simulations of hypervelocity impact of spherical projectiles on targets with rough surfaces (e.g., those with surface boulders and/or undulating topography) revealed smaller cratering efficiency than that formed on flat targets (Susorney et al. 2017; Tatsumi & Sugita 2018), indicating that the encountered geometry of projectiles and target (e.g., irregularly shaped projectiles impacting flat target) has profound implications on impact cratering (Shuvalov 2020). Recent observations revealed that planetary impacts feature frequent changes of ejection azimuths and angles (Xu et al. 2023). The heterogeneous shock impedances caused by irregular shapes of impactor and/or target were invoked as an explanation, which changes the encountering geometry of shock and rarefaction waves (Xu et al. 2023, 2024; Luo et al. 2025). Therefore, the shape of impactors may have profound effect on the formation of simple craters, which may be a cause for the non-uniform morphometry of relatively large lunar simple craters formed in the gravity domain. However, the quantitative effect of irregular shapes of impactors on planetary impacts is not constrained.

In this study, we investigated the effect of impactor shapes on the formation of lunar simple craters. Section 2 describes the method, and the results are shown in Section 3. Section 4 discusses the impact cratering mechanism and implications of the results.

2. Methods

We modelled the formation of lunar simple craters using the iSALE-2D shock physics code (Wünnemann et al. 2006), which is based on the SALE hydrocode (Amsden et al. 1980). iSALE-2D has undergone rigorous validation against experimental studies (Pierazzo et al. 2008). To investigate the effect of impactor shapes on the formation of lunar simple craters, impactors with an identical kinetic energy and impact velocity but different oblateness were modelled. Numerical benchmarks for the DART mission (Owen et al. 2022) and Apollo S-IVB impacts (Rajšić et al. 2021) indicated that simplified geometric models (e.g., spheres or cylinder) yielded reasonable approximations of cratering processes involving irregular impactors (e.g., complex, multi-component spacecraft). With identical densities and thus volumes, the modelled impactors have spherical and ellipsoidal shapes to represent the diverse impactor shapes in the 2D model. The aspect ratio (AR) of the modelled impactors is defined by the ratio between its equatorial (parallel to the pre-impact surface) and polar axes, which are calculated based on the same volume and intermediate axis (Table A.1). The AR values of the modelled impactors vary from 1:1 to 10:1 or 1:10, that AR = 1:1 means spherical impactors and larger AR values represents more oblate impactors. For simplicity, impacts along the long axis (e.g., AR = 1:2) and short axis (e.g., AR = 2:1) of ellipsoidal impactors are hereafter uniformly referred to as 'tapered' and 'flat', respectively. On the basis of empirical impact scaling laws (Schmidt & Housen 1987), the equivalent diameters of impactors (D_p; diameter of ideal spheroid) were set to 20 m, 100 m, and 200 m, corresponding to lunar simple craters with $D \approx$ 400–4000 m, which were formed in the gravity-dominated regime but with prominent morphometric variations (Stopar et al. 2017; Krüger et al. 2018). Impactors with AR $\leq$ 2–4 represent typical oblate rubble-pile asteroids (Hatch & Wiegert 2015; Sugiura et al. 2018) and monolithic fragments (Čapek et al. 2025), while larger ARs denote highly oblate monoliths (Krishna & Kumar 2016). Impact velocity is fixed to 12.7 km s^{-1} in all models, which equals the vertical component of the average lunar impact velocity (18 km s^{-1}; Ivanov 2001) and impact angle of 45°.

We applied uniform target setups in the models (Table A.2) following those applied in simulations for typical lunar simple craters (e.g., Martellato et al. 2017; Li et al. 2025). It is notable that impact cratering processes by impactors with D_p = 20 m to the Moon may be significantly affected by a surface regolith layer (Bart et al. 2011). However, for the purpose of this work, only the impactor oblateness is considered as a model variable. The target was approximated as an infinite half-space under lunar gravity (1.62 m s^{-2}). We used a resolution of 15 cells per projectile radius (CPPR) for spherical impactors, which corresponds to smaller actual grid sizes for oblate impactors (i.e., higher spatial resolution) to compromise the reasonable computation time and sufficient accuracy. The resolution test (Figs. A.1 and A.2) and mesh geometry setups are available in Text A.1.

Both projectile and target materials used the Tillotson equations of state for basalt (Tillotson 1962). Material strength, damage, and thermal softening were accounted for using the models of Collins et al. (2004), Ivanov et al. (2010), and Ohnaka (1995), respectively. The Drucker-Prager (DRPR) strength model (Drucker & Prager 1952) was used to describe the mechanical behaviour of target materials (a description of strength models is available in Text A.2). For the impactors, we used the ROCK strength model to represent high-strength monolithic fragments (Ivanov et al. 2010), which provides a robust approximation for competent impactors (e.g., Martellato et al. 2017; Li et al. 2025). Given that rubble-pile asteroids are substantially weaker and more porous than monolithic impactors (Scheeres et al. 2010), we additionally used the DRPR model with low cohesion (~1 kPa; Raducan et al. 2020, 2022) and a porosity model (Wünnemann et al. 2008) with 20% initial bulk porosity (Naidu et al. 2020; Raducan et al. 2022) to represent rubble-pile impactors (Table A.2) and enable comparison with monolithic impacts (Section 4.2). However, the bulk strength and internal structure of rubble-pile asteroids are poorly constrained (Stickle et al. 2022). Therefore, we conducted additional sensitivity tests to assess the effect of rubble-pile impactor strength

models and cohesion ranges on crater formation (Text A.2; Fig. A.3).

All simulations ran until the final craters formed with stabilised morphometry. The material boundary of the target at the last timestep was extracted as the final crater topography profile. Morphometric parameters were measured from topography profile, including the D, d, d/D ratio, rim height (h), and h/D ratio. Transient craters are defined as excavation cavities when they reach the maximum volume (Wünnemann et al. 2011). Their diameter (D_t) and depth (d_t) are measured relative to the pre-impact surface. Cratering efficiency (π_v) is defined as the mass ratio between materials originally contained within the transient crater and the impactor (Schmidt & Housen 1987; Holsapple 1993).

Lagrangian tracers are used to track the trajectories, provenance, and shock history of excavated materials. Tracers, inserted in each computational cell, represent the initial material position in the simulation and move along with the velocity field of the material flow. They record the pressure field at each timestep and peak shock pressure experienced upon shock compression. At the final timestep, we recorded the positions of tracers within deposits on crater rims (i.e., ejecta deposited above the pre-impact surface) and traced their initial positions and peak shock pressures experienced. In addition, we tracked the propagation of the shock wave and rarefaction waves in both the impactor and target during the early stage of impact cratering. The arrival time of the shock wave front is defined as the time when the pressure of each tracer exceeds 1 GPa from the undisturbed state (Kurosawa et al. 2018). The arrival time of the rarefaction wave front is calculated to be the time when the pressures of the shocked tracers decrease to one-third of the peak pressures (Kurosawa et al. 2018).

We investigated the effect of impactor oblateness on melt production by calculating the amount of materials experiencing peak shock pressures exceeding 60 GPa (Hamann et al. 2016). The total melt production is the sum of all tracer masses with peak shock pressures exceeding 60 GPa (e.g., Manske et al. 2021; Liu et al. 2022). The impact melt volume (V_m) is calculated by dividing the total melt mass by the initial density of the tracer material (details see Text A.3). We employed 80–120 CPPR for all the models (Table A.3) to determine the impact-induced melt volume (resolution tests are available in Fig. A.4). For this purpose, only the early stage of the impact process (i.e., before the shock pressure attenuates to <60 GPa) was modelled (e.g., Wünnemann et al. 2008; Halim et al. 2021).

3. Results

3.1. Effect of impactor oblateness on crater morphology

Our numerical simulations show that impactor oblateness affects lunar simple crater morphologies. With identical initial kinetic energy, spherical impactors (Figs. 1a, A.5a, and A.6a) produce typical bowl-shaped craters (Figs. 1j, A.5g, and A.6g), whereas increasing impactor oblateness induces morphological changes from normal bowl-shape to either flat-bottomed (Figs. A.5h and A.6h) or conical-shaped (Figs. A.5i and A.6i) craters, depending on the impact direction along either the short or long axis of the impactor, respectively (Figs. 1, A.5, and A.6; Table A.4). For flat impacts (i.e., AR ≥ 2:1), larger impactor AR causes both smaller final crater depth and diameter than those formed by spherical impactors, with reductions of ~1–6% when AR = 2:1 to ~10–14% when AR = 10:1 (Fig. 1m). By contrast, tapered impacts (i.e., AR ≥ 1:2) drive substantially larger reductions in both d and D than flat impacts (Fig. 1m). When AR increases from 1:2 to 1:10 for different-sized impactors, d decreases from ~11–16% to ~27–29% and D from ~11–16% to ~45–48% (Fig. 1m).

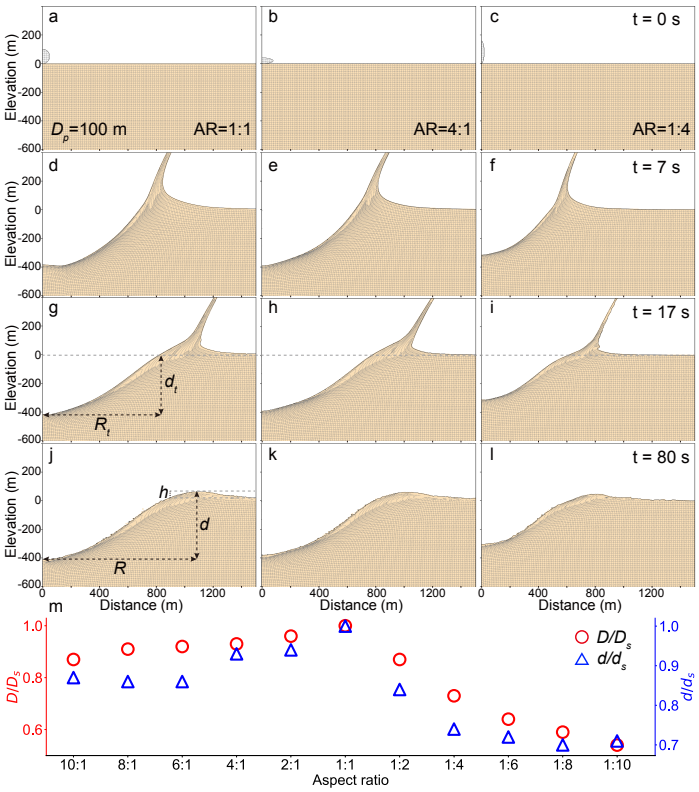

Fig. 1: Snapshots of formation process of lunar simple craters by spherical impactor with D_p = 100 m (left column) and oblate impactors with equivalent kinetic energy (aspect ratio, AR = 4:1, middle column; AR = 1:4, right column). The horizontal and vertical grey lines represent the deformation of the materials. The dashed grey lines in panels (g–i) donates the pre-impact surface. Measurements of transient crater (g) and final crater (j) morphometry are annotated using dashed arrows, including rim-to-floor depth (d), rim crest radius (R), rim height (h), transient crater depth (d_t) and radius (R_t). Transient craters form after approximately 17 s (g–i). (m) Larger impactor AR yields both smaller final crater depth and diameter relative to spherical impactors (i.e., d/d_s and D/D_s, shown as blue triangles and red circles, respectively).

3.2. Effect of impactor oblateness on morphometric parameters

While larger impactor oblateness yields smaller depths, diameters, and rim heights of final craters (Figs. 2a, 2d, and 2g), the effect of impactor AR on critical ratios of morphometric parameters (i.e., d/D and h/D ratios) is negligible (Fig. 2), except for tapered impacts by extremely oblate impactors (e.g., AR ≥ 1:6). For impactor oblateness ranging from 1:4 to 10:1, d/D ratios are still around 0.21 (Figs. 2b, 2e, and 2h) and h/D ratios are about 0.03 (Figs. 2c, 2f, and 2i), aligning with typical morphometric characteristics of lunar simple craters (Pike 1974, 1977; Fassett & Thomson 2014). Therefore, both d/D and h/D ratios exhibit no systematic or significant variations with respect to AR values. Notably, for tapered impacts, extreme impactor oblate-

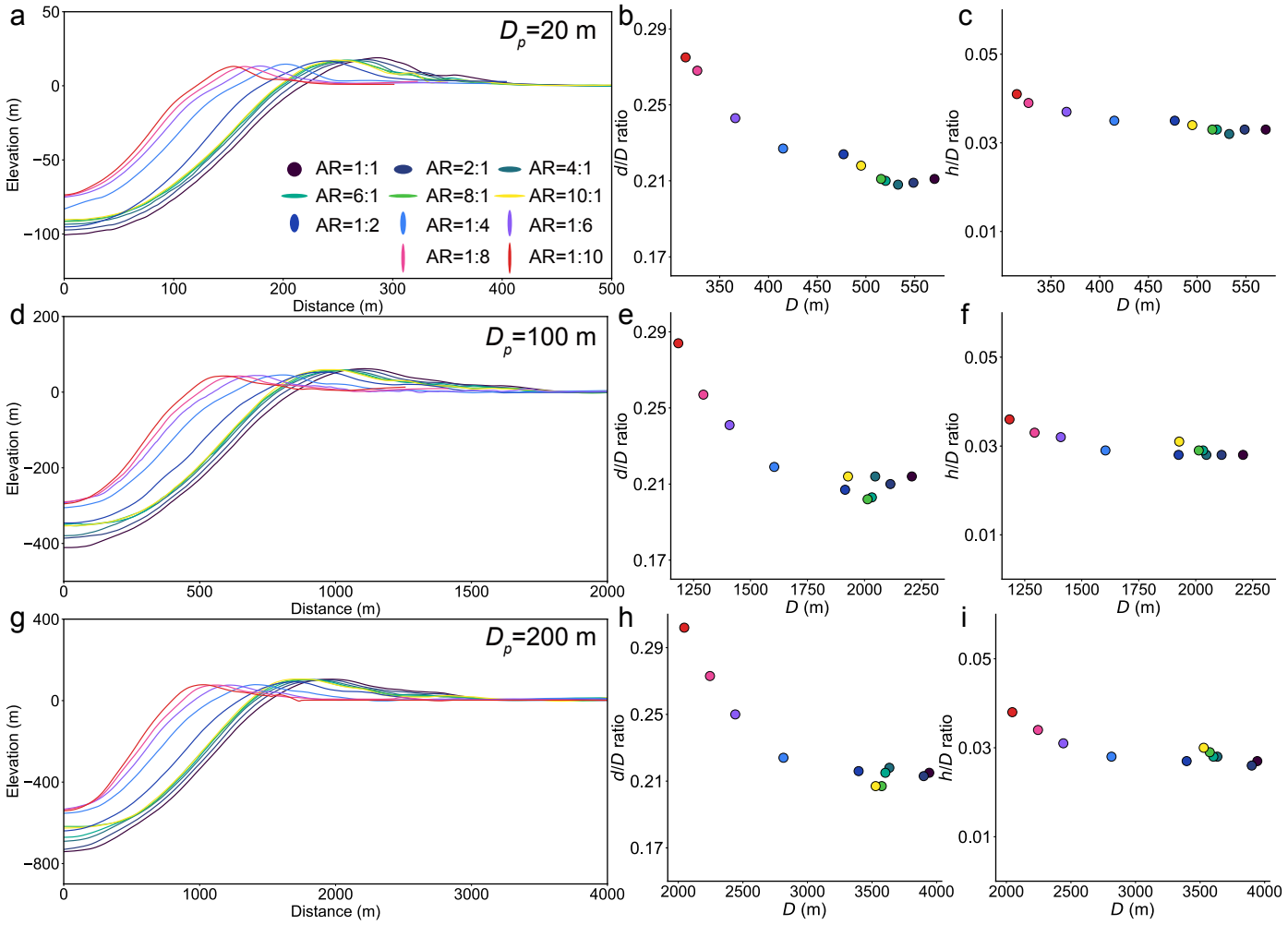

Fig. 2: Effect of impactor oblateness (AR) on the morphology and morphometry of lunar simple craters with equivalent projectile diameters (i.e., same initial kinetic energy) of D_p = 20 m (a–c), 100 m (d–f), and 200 m (g–i). (a, d, g) Profiles of modelled craters with varying impactor oblateness (see legend). (b, e, h) d/D ratios of modelled craters. (c, f, i) h/D ratios of modelled craters.

ness (AR ≥ 1:6) yields significantly smaller d/D ratios (Figs. 2b, 2e, and 2h). Therefore, our results suggest that oblate impacts do not produce extremely shallow (e.g., $d/D \leq 0.16$) or deep (e.g., $d/D \geq 0.25$) simple craters as observed on the Moon (e.g., Stopar et al. 2017), except for impactors with extreme oblateness, i.e., AR ≥ 1:6 for both flat and tapered impacts.

3.3. Effect of impactor oblateness on cratering efficiency

Compared to transient cavities formed by spherical impactors, those formed by impactors with greater oblateness are smaller and shallower transient craters (Fig. 3; Table A.4). The incidence direction of oblate impactors also modulates dimensions of transient craters, with tapered impacts producing consistently smaller depths (d_t), diameters (D_t), and volumes (V_t) of transient craters than flat impacts. For all modelled impactor sizes (i.e., D_p = 20–200 m), as impactor AR increases from 1:1 to 10:1 (i.e., flat impacts), D_t decreases by ~4% to ~10%, and d_t decreases by ~1–6% to ~10–17% (viridis profiles in Figs. 3a–3c), resulting in a reductions of V_t by ~8% (AR = 2:1) to ~22% (AR = 10:1). When the AR of different sized impactors changes from 1:1 to 1:10 (i.e., tapered impacts), D_t decreases by ~14–17% to ~44–47%, and d_t decreases by ~7–17% to ~26–27% (blue-to-red profiles in Figs. 3a–3c), yielding reductions of V_t by ~38% (AR = 1:2) to ~80% (AR = 1:10).

For both flat and tapered impacts, the cratering efficiency exhibits a non-linear decline with increasing impactor oblateness (Figs. 3d–3f). Cratering efficiency decreases quickly when the impactor aspect ratio increases from 1:1 to 4:1 or 1:4, and it reduces more slowly at larger AR values (Figs. 3d–3f; Table A.4). For example, compared to spherical impacts (π_v = 1597 for D_p = 20 m; π_v = 752 for D_p = 100 m; π_v = 540 for D_p = 200 m), π_v decreases by approximately 8%, 16%, 19%, 21%, and 22% for flat impacts with AR = 2:1, 4:1, 6:1, 8:1, and 10:1, respectively, and by about 38%, 63%, 73%, 77%, and 80% for tapered impacts with AR = 1:2, 1:4, 1:6, 1:8, and 1:10.

3.4. Effect of impactor oblateness on the provenance of rim crest ejecta

Ejecta deposits on rim crests of simple craters are a common reference for deducing the composition of materials excavated from the maximum excavation depth (e.g., Wang et al. 2024). By tracking the initial position of materials deposited on rims of the modelled craters, we tracked the provenance of ejecta excavated from transient cavities (Fig. 4a). The maximum original depths of ejecta on crater rims are approximated as the maximum exca-

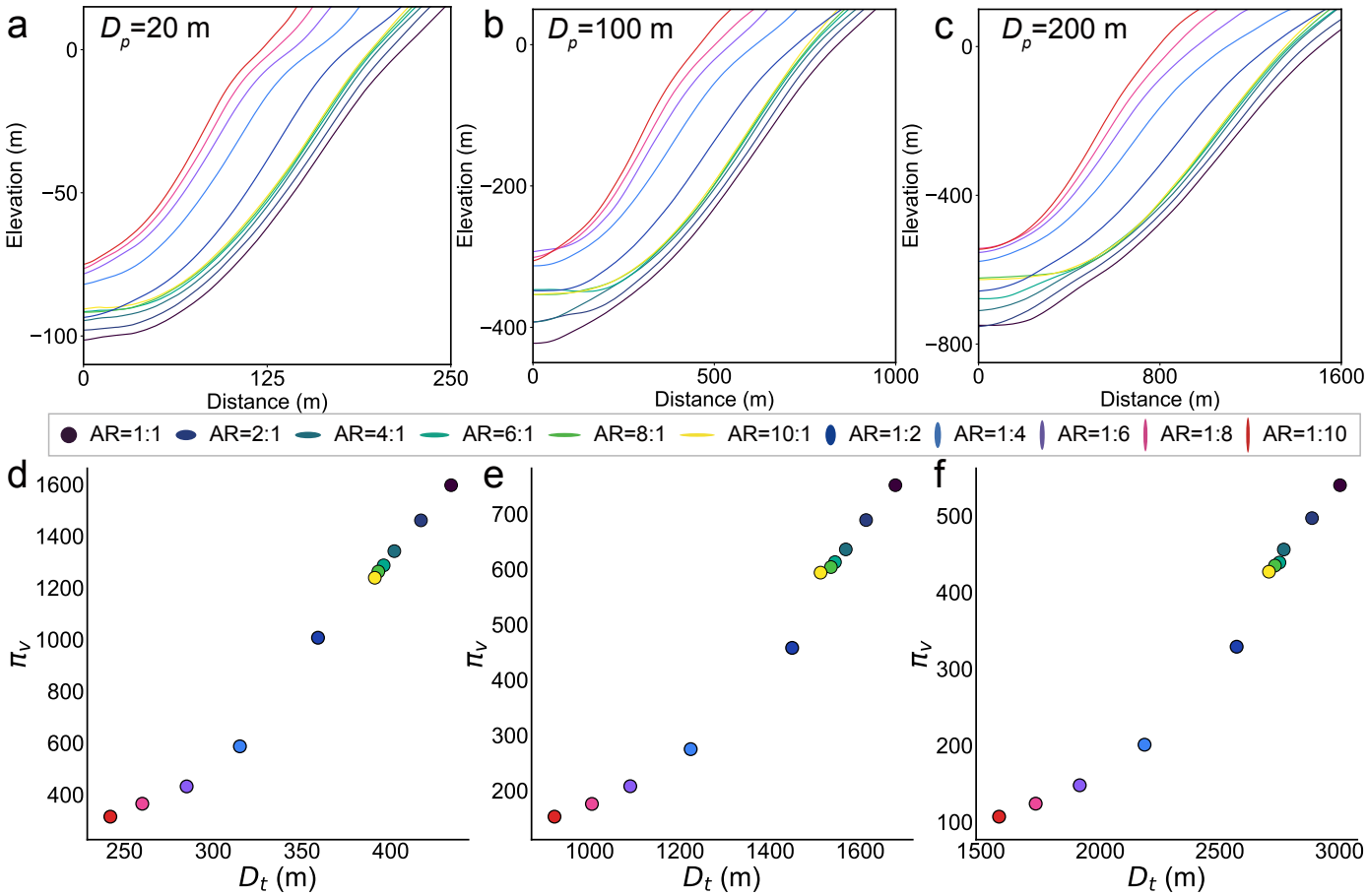

Fig. 3: Effect of impactor oblateness on transient crater morphometry and impact cratering efficiency. Impactors with equivalent projectile diameters (i.e., same initial kinetic energy) of D_p = 20 m (a, d), 100 m (b, e), and 200 m (c, f) but varying aspect ratios (1:1 to 10:1 and 1:10). (a–c) Profiles of transient craters. (d–f) Transient crater diameter (D_t) and cratering efficiency (π_v) decrease with increasing impactor oblateness.

vation depths (d_{exc_max}) during the formation of transient cavities (Fig. 4a). Shallower materials were sources of more distal impact ejecta, and deeper materials were displaced downwards (Melosh 1989). For both flat and tapered impacts, with larger impactor oblateness, impact ejecta were generally excavated from shallower depths (Fig. 4a), with d_{exc_max} decreasing by up to ~22% relative to that of spherical impacts (Fig. 5; Table A.5). However, for tapered impacts, extreme impactor oblateness (i.e., AR ≥ 1:6) did not yield increasingly smaller d_{exc_max}, but it did rise slightly at larger AR values (Fig. 5). When AR changes from 1:1 to 10:1 (or 1:10), the ratios of d_{exc_max}/d_t and d_{exc_max}/d increased from approximately 0.44 and 0.38 to 0.47–0.52 and 0.41–0.46, respectively (Fig. 4b; Table A.5). Notably, the normalised maximum excavation depths remain nearly constant for ARs of less than 4:1 and 1:4 (Fig. 4b).

4. Discussion

4.1. Impact cratering mechanism by oblate impactors

During the contact and compression stage, spherical impactors produce a roughly hemispherical high-pressure field and sustain high-pressure zones near the impact point (Fig. 6a). Rarefaction waves caused by reflection of shock waves from free surfaces quickly catch the expanding shock wave, releasing the high pressure of shocked materials and imparting additional particle velocities (Fig. 7a; Gault et al. 1968; Melosh 1989), and triggering the excavation flow. Compared to spherical impacts, flat impacts (i.e., AR ≥ 2:1) form an elliptical high-pressure field with respect to the target surface, broader near-surface high-pressures zones (e.g., >60 GPa; Figs. 6b and 6c), but smaller intermediate (>20 GPa) and low-pressure (>5 GPa) zones (Fig. 6f), suggesting faster shock wave attenuation in the target. On the contrary, tapered impacts produce narrower and elliptical high-pressure fields along the impact direction (Figs. 6d and 6e), forming significantly smaller pressure zones in both depths and lateral scales than those of spherical and flat impacts (Fig. 6f). Therefore, for impactors with identical kinetic energy, a larger oblateness yields energy transfer to limited target regions and accelerates shock wave attenuation, yielding less energy for impact excavation, and thus reducing the excavation depth and cratering efficiency.

The effective contact area (i.e., footprint) between oblate impactors and target during the initial contact and compression stage are a fundamental cause for the behaviour of shock decay (Raducan et al. 2022; Wu et al. 2026). Compared to spherical impactors, tapered impactors have much smaller effective contact areas with the target by up to about 21 times (Table A.1), causing concentrated energy release beneath the impact point, deeper penetration depths (Wu et al. 2026), and confinement of high-pressure zones to narrower regions along the incidence direction (Figs. 6d and 6e). In contrast, flat impactors

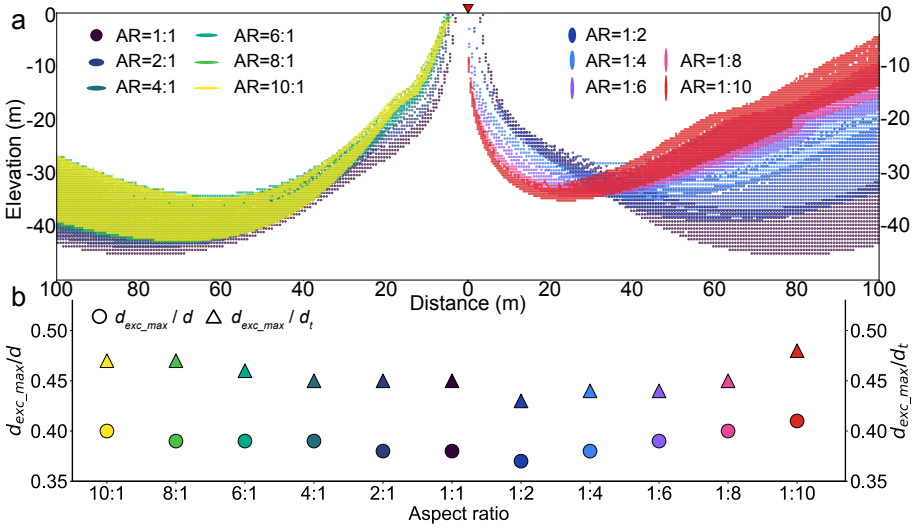

Fig. 4. Effect of impactor oblateness on the provenance of ejecta that deposit on rim crests. (a) Provenance of ejecta deposited on crater rims for impactors with D_p = 20 m but varying ARs of 1:1 to 10:1 (left) and 1:10 (right). Dots show Lagrangian tracers implanted in the models. Maximum excavation depths (d_{exc_max}) decrease with larger impactor oblateness. (b) Maximum excavation depths normalised to final crater depth (d) and transient crater depth (d_t) are nearly identical for low impactor oblateness (i.e., AR ≤ 4:1 or 1:4), but they increase under extreme oblateness (e.g., AR = 10:1 or 1:10). The relationship between ejecta provenance and impactor oblateness holds for impactors with different sizes, e.g., the results for D_p = 100 m and 200 m are available in the Zenodo repository.

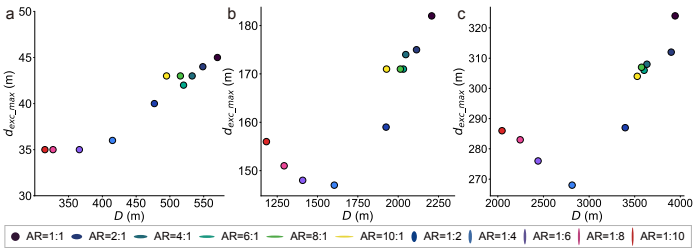

Fig. 5: Effect of impactor oblateness on maximum excavation depths (d_{exc_max}) of ejecta on the crater rim. Impactors with equivalent D_p = 20 m (a), 100 m (b), and 200 m (c) but varying aspect ratios (1:1 to 10:1 and 1:10).

have much larger footprints (up to fivefold increases; Table A.1), and the impact energy is released to a restricted area near the surface (Raducan et al. 2022), producing broader near-surface high-pressure zones (Figs. 6b and 6c). Therefore, less energy is available for the excavation of the transient crater (Oberbeck 1971; Melosh 1989), reducing the cratering efficiency (e.g., Elbeshausen et al. 2013).

For oblate impactors with different ARs, the different attenuation rates of shock waves in the target arise from the spatial and temporal differences in the interaction between shock waves and rarefaction waves. For flat impacts, the upwards-propagation path of the shock wave within the impactor is shorter than that for spherical impactors. Rarefaction waves are generated at the rear surface of the flat impactor more rapidly, causing faster attenuation of shock waves (Fig. 7c). For tapered impacts, shortly after shock wave formation, rarefaction waves are generated at the highly deformed front edge of the impactor and the free surface of the target (hereafter edge waves; Nakazawa et al. 2002), propagating both upward within the impactor and downward into the target, respectively (Fig. 7b). Upward-propagating edge waves unload the shocked impactor much faster than those formed by spherical or flat impacts (Fig. 7b), yielding more efficient dissipation of the impactor kinetic energy. This is consistent with previous findings that larger impactor footprints yield higher melt fractions (Potter & Collins 2013) and lower cratering efficiency (Rajšić et al. 2021). Meanwhile, edge waves propagate through the target and catch the shock waves much faster than reflected rarefaction waves, causing earlier and faster attenuation of the shock waves (Fig. 7b). Consequently, tapered impacts exhibit significantly lower cratering efficiency (Fig. 3) and smaller excavation depths (Fig. 5) than both spherical and flat impacts.

During the excavation stage, the encountered geometry of shock and rarefaction waves alter the velocity field of excavation flows (Maxwell 1977). Our model shows that the geometry of excavation flows formed by oblate impactors is distinct from that formed by spherical impactors. Flat impacts generate approximately parallel shock and reflected rarefaction waves across a broad region beneath the impact point (Fig. 7c), displacing more target materials downwards to the crater floor rather than forming more ejecta. As impactor oblateness increases (AR = 2:1–10:1), impact ejecta are excavated from regions farther from the impact point (e.g., Fig. 4b), and the crater floor morphology gradually changes from bowl shaped to flat bottomed (Figs. 2, A.5, and A.6). In contrast, for tapered impacts, the angle between the propagating directions of shock and edge wave fronts becomes larger (Fig. 7b) beneath the impact point, causing more target materials to be excavated than displaced. Therefore, when the impactor AR values increase from 1:2 to 1:10, tapered impacts yield larger excavation depths and conical crater morphology (Figs. 2, A.5, and A.6), and impact ejecta are from regions closer to the impact point (Fig. 4a). While this work emphasises the effect of impactor oblateness on impact ejection and geometry of transient cavities, the model predictions are based on simplified model assumptions such as vertical impacts and homogeneous target properties. It is notable that planetary impacts usually feature much more complicated impact conditions that may affect impact excavation, such as surface topographic undulations and subsurface structural discontinuities (e.g., Tatsumi & Sugita 2018; Xu et al. 2023).

4.2. Geological implications

Our results show that the irregular shape of typical near-Earth objects (NEOs), with AR values less than 4:1 or 1:4, does not account for the variations of morphometric parameters (e.g., d/D and h/D ratios) of pristine primary simple craters with D = 400–4000 m on the Moon. Impactor oblateness does not affect the empirical scaling relationships between the maximum excavation depth and crater geometries (e.g., $d_{exc\_max} = 0.1D_t$; Croft 1980) either (Figs. 2 and 4). Therefore, our results uphold the credibility of using lunar simple crater morphometries as geological proxies for subsurface structure and composition. Mean-

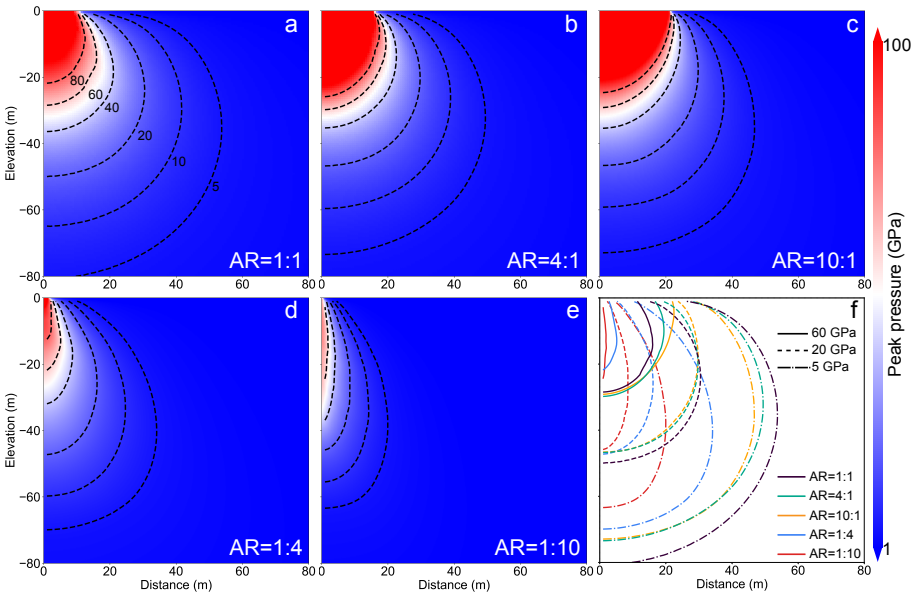

Fig. 6. Peak shock pressure distribution for impact events with impactor equivalent diameters (D_p) of 20 m and varying ARs. Tracers are displayed at their initial position for better visibility of peak pressure distribution. Contour lines of peak pressure are donated by dashed black lines with values of 80 GPa, 60 GPa, 40 GPa, 20 GPa, 10 GPa, and 5 GPa displayed sequentially from the impact point outwards. (a) AR = 1:1. (b) AR = 4:1. (c) AR = 10:1. (d) AR = 1:4. (e) AR = 1:10. (f) Comparison of the 60 GPa, 20 GPa, and 5 GPa peak pressure contour lines. Results for impactors with D_p = 100 m and 200 m are available in the Zenodo repository.

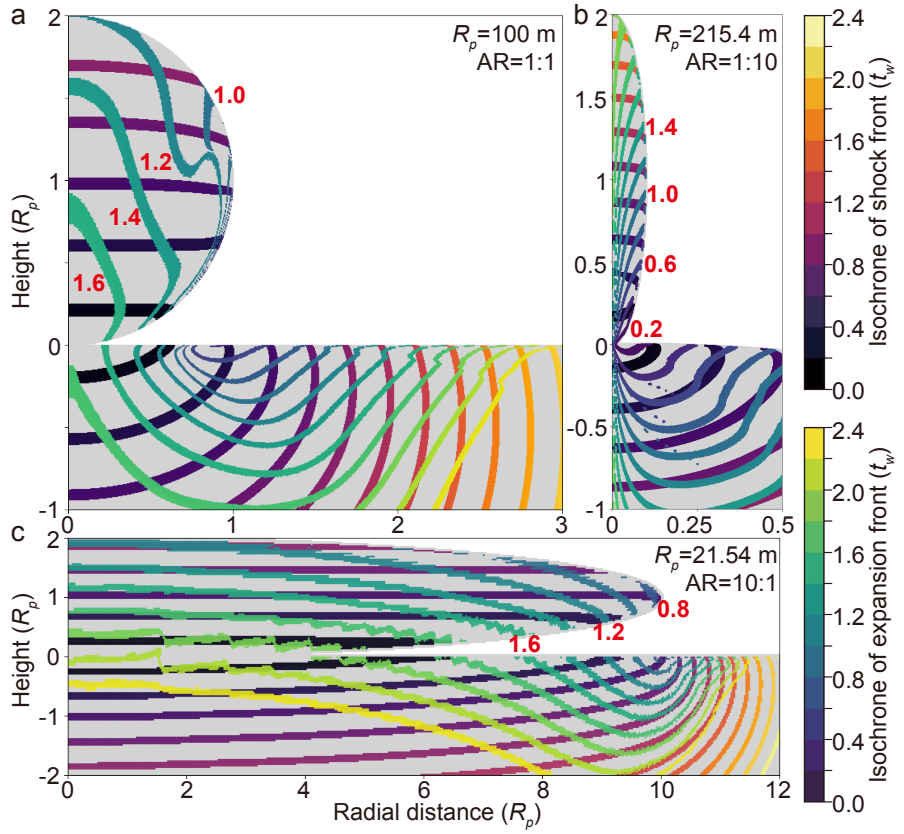

Fig. 7. Isochrones of the shock front (black-to-yellow) and rarefaction wave front (viridis) for impact events with D_p = 200 m and varying impactor aspect ratios of 1:1 (a), 1:10 (b), and 10:1 (c). Wave fronts are plotted as the initial position of each tracer. The arrival times of the shock front and rarefaction wave front are defined as the time when the pressure of each tracer exceeds 1 GPa from the undisturbed state, and the time when the pressure of a shocked tracer decreases to one-third of the peak pressure, respectively (Kurosawa et al. 2018). Tracer positions and wave arrival times (t_w = 2 × R_p / v) are normalised by the impactor polar radius (R_p) and the impact velocity (v). Red digital labels denote scaled rarefaction wave isochrones in the impactors. For spherical (a) and flat (b) impacts, rarefaction waves form later at the impactor's rear surface and propagate downwards. For tapered impacts (c), rarefaction waves form immediately after the moment of impact and propagate upwards into the impactor from its front edge. The horizontal-to-vertical axis ratios are equal for panels (a) and (c), while panel (b) exhibits a 2:1 ratio for better visualisation of wave fronts in the impactor.

while, the results show that the shape of NEOs were not directly recorded in the morphometry of lunar simple craters.

By tracking the shock states of rim deposits, our results show that that most of them are lithic fragments that experienced shock pressures below 60 GPa (Fig. 8). For all tested impactor sizes and oblateness, only ~1–2 vol.% of ejecta deposits on rim crests are impact melt (Table A.5). Therefore, impactor oblateness has a negligible effect on the abundance of impact melt on rims of lunar simple craters. This is consistent with the minor occurrences of melt-rich ejecta deposits on rims of lunar pristine simple craters (Plescia & Cintala 2012). Our modelling results further show that impactor oblateness has minor effect on the provenance distribution of crater rim materials, which are consistently sourced from depths of 0 to ~0.4d (Fig. 8b). This result further verifies the robustness of lunar simple craters as natural probes for constraining ejecta provenance.

Impactor oblateness affects the size of high-pressure zones (e.g., peak shock pressures exceed 60 GPa; Fig. 6), thus modulating the volume of impact melt (Fig. 9). Our modelled results show that for lunar simple craters with D = 400–4000 m, formed by typical NEOs (i.e., AR ≤ 4:1–1:4), the volume of impact melt produced varies by up to approximately 25 times (Fig. 9; Table A.5), whereas the crater volumes vary by less than 3 times (Table A.5), with similar crater morphom-

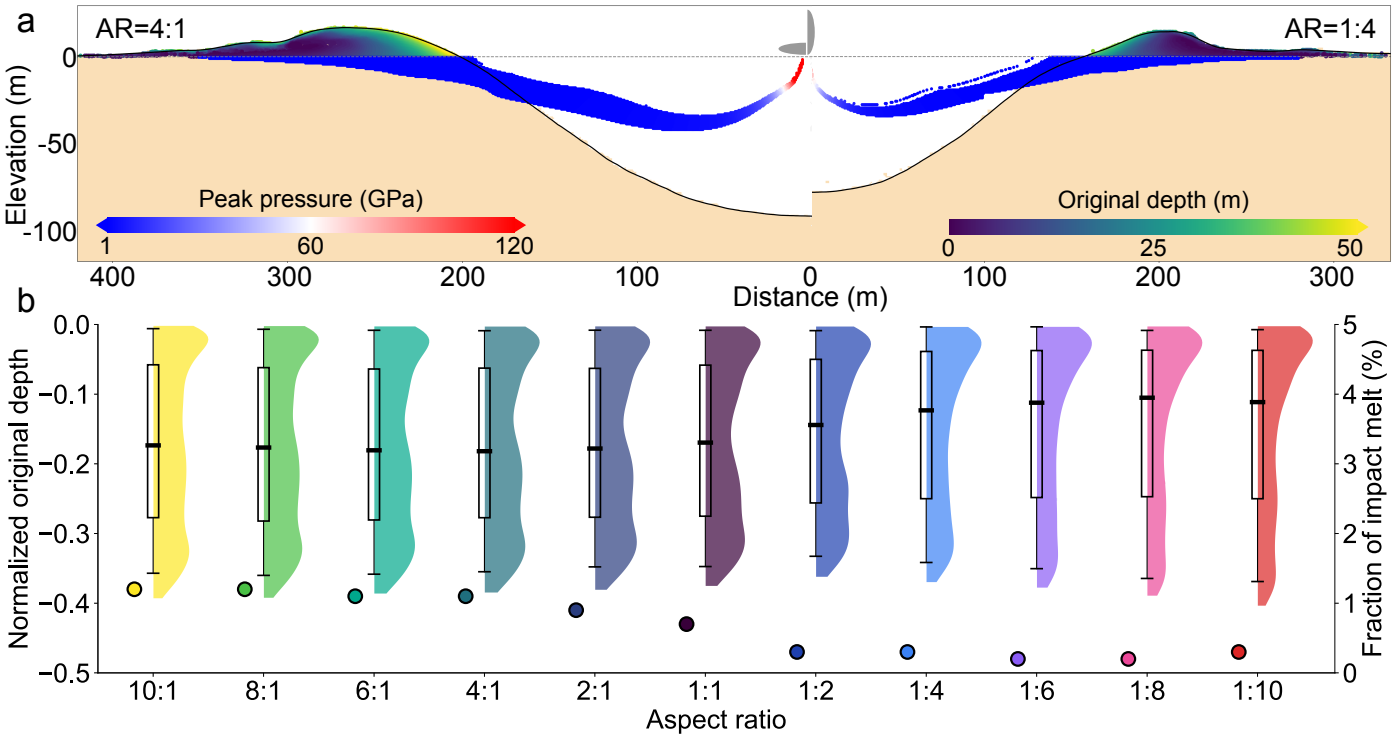

Fig. 8: Shock states and original depths of crater rim materials for impact events with equivalent D_p = 20 m and varying impactor oblateness (AR). (a) Original depths of modelled crater rim materials (colour-coded by viridis scale). Lagrangian tracer particles showing initial locations and peak shock pressures (blue-to-red scale) of crater rim materials. Left and right panels compare oblate impactor scenarios with AR = 4:1 and 1:4, respectively. (b) Statistics of original depths of final crater rim materials (above the pre-impact surface) of modelled craters with varying ARs. Inset violin plots show the probability density distribution of normalised original depths, which are the original depth divided by the final crater depth. The median normalised original depth is indicated by a horizontal black line. The 25th and 75th percentiles are represented by black boxes, and the 5th and 95th percentiles are marked by vertical black lines. The right vertical axis and dots represent the fraction of impact melt in crater rim materials. Colours denote impactors with varying aspect ratios. Results for impactors with D_p = 100 m and 200 m are available in the Zenodo repository.

etry. This range of modelled impact melt volume is generally consistent with the trend of existing melt scaling laws (e.g., Cintala & Grieve 1998; Liu et al. 2022). By affecting the geometry of excavation flow (Fig. 4a) and the spatial distribution of melt within the target (Fig. 6), non-spherical impactors would further yield different partitioning of impact melt between crater interiors and ejecta compared to spherical impactors. This effect may explain the observed variations of impact melt abundances within sub-kilometer- to kilometer-sized lunar simple craters (Plescia & Cintala 2012; Stopar et al. 2014).

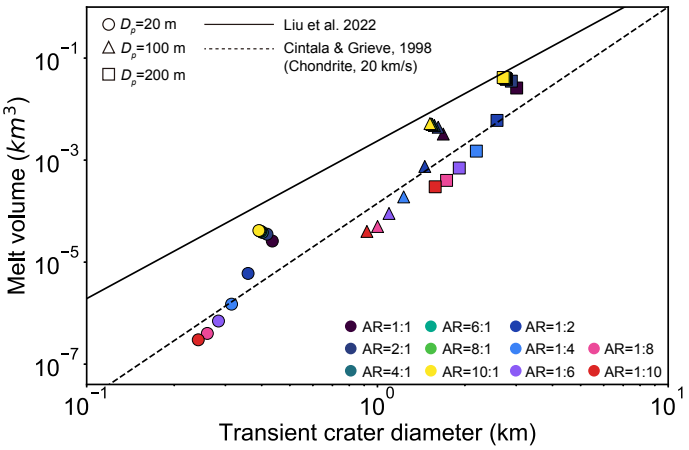

Fig. 9: Effect of impactor oblateness on total impact melt volume with comparison of existing scaling laws. Total melt volume increases by ~1.6 times as the impactor AR increases from 1:1 to 10:1, and decreases by ~2 orders of magnitude as AR varies from 1:1 to 1:10. Our modelled results fall within the trendlines of two scaling laws from Cintala & Grieve (1998) (dashed line) and Liu et al. (2022) (solid line), except for extreme tapered impactors (i.e., AR > 1:4). Compared with modelled melt scaling from Liu et al. (2022), our models do not incorporate target porosity, which tends to underestimate the actual impact melt production (Wünnemann et al. 2008)

Near-Earth asteroids with diameters of several hundreds meters are likely rubble-pile asteroids, which are loosely bound aggregates with low bulk cohesion and high porosity (Michel et al. 2001). Compared to impacts by high-cohesion dense monolithic fragments, impacts by rubble-pile asteroids yield crater depths and diameters that are proportionally smaller by ~6% (Fig. 10; Table A.6), while the cratering efficiency increases by ~6% (Table A.6). However, crater morphology (Figs. 10a and 10b) and morphometry (e.g., d/D ratio; Fig. 10e) remain unchanged. Therefore, our results suggest that the morphology of primary simple craters on the Moon is insensitive to the physical properties of impactors.

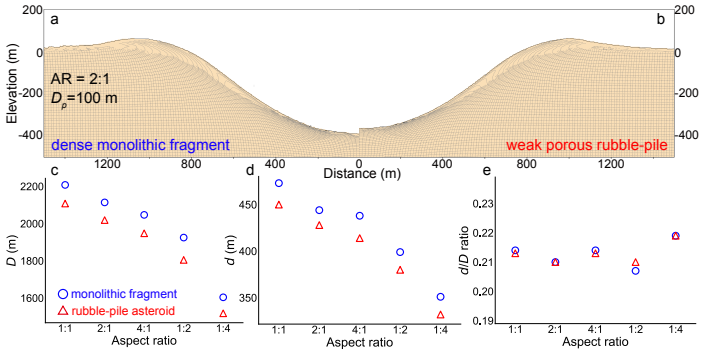

Fig. 10: Comparison of morphology (a, b) and morphometry (c–e) of lunar simple craters formed by dense monolithic fragments (blue) and rubble-pile asteroids with 20% bulk porosity (red). (a, b) Snapshots of final craters formed by monolithic fragment (left panel) and rubble-pile (right panel) with D_p = 100 m and AR = 2:1. The rubble-pile asteroid was modelled using the DRPR strength model with cohesion of 1 kPa. Variations in strength model (i.e., DRPR or ROCK model) and cohesions (i.e., 0.1–10 kPa) of rubble-pile asteroids have negligible effects on crater morphometries (Fig. A.3; Table A.6). The horizontal and vertical grey lines represent the deformation of the materials. (c–e) Effect of impactor physical properties (i.e., cohesion and porosity) on crater diameter (c), depth (d), and d/D ratio (e), with D_p = 100 m but varying AR (1:1 to 4:1 and 1:4).

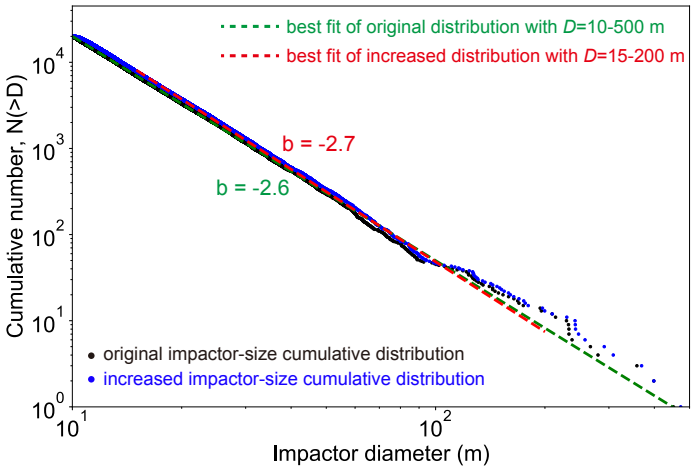

Fig. 11: Effects of irregular impactors on the cumulative size distribution of NEOs. Black dots denote the original cumulative size distribution of 20000 randomly generated NEOs with equivalent diameters of 10–500 m following a power-law relationship with slope b = -2.6 (dashed green line). Blue dots show the cumulative size distribution after randomly increasing each impactor's equivalent diameter by 0–18% to account for reduced cratering efficiency of irregular shapes. The best-fit power-law slope for the adjusted impactor distribution with diameters of 15–200 m is -2.7 (dashed red line). The vertical axis represents the cumulative number of impactors with diameters greater than D, i.e., $N(>D)$.

4.3. Slope estimation of the cumulative size distribution of NEOs

Impactors forming primary simple craters with D = 400–4000 m are mainly NEOs (Neukum et al. 2001) with non-spherical shapes (Holsapple 2001). The cumulative size-frequency distribution (SFD) of lunar simple craters with diameters larger than D follows a power-law form of $N(>D) \propto D^b$, where b denotes the power-law slope (Neukum et al. 1975). On the basis of the observed SFD of lunar simple crater populations and empirical scaling laws, the cumulative size distribution (i.e., without area normalisation) of NEOs (i.e., causative impactors) has been assumed to follow the same power-law form with b = -2.6 (e.g., Marchi et al. 2009; Xie et al. 2021). Notably, the population of decameter-sized NEOs remains poorly constrained (Harris & D'Abramo 2015), we assume that NEOs in the tens to hundreds of meters also adhere to the same power-law distribution (dashed green line, Fig. 11).

Given the reduced cratering efficiency caused by non-spherical impactors (Section 3.3), a given-sized simple crater would need a larger oblate impactor than predicted by empirical scaling for spherical projectiles. For an AR of 2:1 or 1:2 (i.e., over half of NEOs have AR ≤ 2:1; Sugiura et al. 2018), the causative impactors should be ~9–64% larger in volume, i.e., ~3–18% larger in equivalent spherical diameter (Table A.4). To quantify this effect and refine the slope of NEO distribution, we randomly generated 20000 impactors with diameters of 10–500 m (black dots, Fig. 11), corresponding to lunar simple craters with $D \approx$ 300 m – 10 km, with power-law slope of -2.6. Each impactor diameter was then scaled by a random increment between 0 and 18%, sampled from a positive half-normal distribution with a mean value of zero and a standard deviation (σ) of 6% (i.e., 3σ = 18%). From the adjusted impactor populations (blue dots, Fig. 11), the revised slope of the size distribution of impactors with diameters of 15–200 m (i.e., craters with $D \approx$ 400–4000 m; dashed red line, Fig. 11) is -2.7, which is ~3.8% steeper than prior estimates (Marchi et al. 2009; Xie et al. 2021).

Our results may explain why the observed number of NEOs with a diameter of 10s–100s meters exceeds estimates from lunar crater populations (Werner et al. 2002), and discrepancies between the model production function (MPF; Marchi et al. 2009) and the Neukum production function (NPF; Neukum et al. 2001) for young lunar surfaces. Furthermore, if the steeper impactor SFD indicates an increased impact flux of NEOs with diameters of tens to hundreds of meters, it is likely that more objects may originate from catastrophic disruptions of main-belt asteroids (e.g., Bottke et al. 2007) and/or the tidal disruption of NEOs during close encounters with Earth (Granvik & Walsh 2024).

5. Conclusion

We conducted numerical simulations to investigate the effects of impactor oblateness on the formation of lunar simple craters. Our results reveal that increasing the impactor aspect ratio from 1:1 (spherical) to 10:1 (flat) or 1:10 (tapered) reduces final crater depth and diameter by up to ~30% and ~50%, respectively. These changes are accompanied by morphological transitions from bowl-shaped to flat-bottomed or conical-shaped, decreases in maximum excavation depth of up to ~22%, and reductions in cratering efficiency by up to ~80%. However, critical morphometric parameters (e.g., d/D ratio) remain invariant across most aspect ratios, especially for typical NEOs (AR ≤ 1:4–4:1), indicating that impactor oblateness is not responsible for the morphometric variability in gravity-dominated lunar simple craters and that crater morphology is not a diagnostic indicator of impactor shape. Furthermore, impactor oblateness has negligible effects on the provenance (~0–0.4d) or impact melt fraction (<2 vol.%) of ejecta deposited on crater rim crests, confirming that

lunar simple craters remain reliable natural probes of subsurface structure and composition. Impactor oblateness affects the sizes of peak shock pressure zones, yielding variations in total impact melt volume spanning up to two orders of magnitude. These disparities arise from the earlier generation of rarefaction waves for oblate impacts, which accelerates shock energy dissipation and reduces the cratering efficiency. Our results also provide new insights into reconciling discrepancies between the size distribution of observed NEOs and that inferred from lunar simple crater populations.

Acknowledgements. The manuscript was improved thanks to comments provided by Andrea Rajšić. The authors gratefully acknowledge the developers of iSALE (www.isale-code.de), including Gareth Collins, Kai Wünnemann, Dirk Elbeshausen, Boris Ivanov, and Jay Melosh and the developers of pySALEPlot including Tom Davison. The authors are supported by the National Natural Science Foundation of China (42508001, 42241108, 62227901, 423B2205), the Postdoctoral Fellowship Program (grant GZB20240881), and the fellowship of the China Postdoctoral Science Foundation (2024M763739).

6. Data Availability

This work has been produced using the iSALE shock physics hydrocode. At present, iSALE is not fully open source. Application for use of iSALE can be made via https://isale-code.github.io/. Any recent stable release can be used to reproduce the data presented. The iSALE-2D input files used to generate simulations, simulation results and videos are available in the Zenodo repository: `https://doi.org/10.5281/zenodo.19589830`

References

Amsden, A. A., Ruppel, H. M., & Hirt, C. W. 1980, SALE: A simplified ALE computer program for fluid flow at all speeds, LA-8095
Bart, G. D., Nickerson, R. D., Lawder, M. T., et al. 2011, Icarus, 215, 485
Bottke, W. F., Vokrouhlický, D., & Nesvorný, D. 2007, Nature, 449, 48
Čapek, D., Petřík, M., Pachman, J., et al. 2025, A&A, 696, A40
Cintala, M. J. & Grieve, R. A. F. 1998, Meteor. Planet. Sci., 33, 889
Croft, S. K. 1980, in Lunar Planet. Sci. Conf., 3, 2347
Collins, G. S., Melosh, H. J., & Ivanov, B. A. 2004, Meteor. Planet. Sci., 39, 217
Drucker, D. C., & Prager, W. 1952, Q. Appl. Math., 10, 157
Elbeshausen, D., Wünnemann, K., & Collins, G. S. 2013, J. Geophys. Res.: Planets, 118, 2295
Fassett, C. I. & Thomson, B. J. 2014, J. Geophys. Res.: Planets, 119, 2255
Gault, D. E., Quaide, W. L., & Oberbeck, V. R. 1968, in Shock Metamorphism of Natural Materials, ed. B. M. French, & N. M. Short, 87
Granvik, M. & Walsh, K. J. 2024, ApJ, 960, L9
Halim, S. H., Crawford, I. A., Collins, G. S., et al. 2021, Icarus, 354, 114026
Hamann, C., Luther, R., Ebert, M., et al. 2016, Geophys. Res. Lett., 43, 10602
Harris, A. W. & D'Abramo, G. 2015, Icarus, 257, 302
Hatch, P. & Wiegert, P. A. 2015, Planet. Space Sci., 111, 100
Holsapple, K. A. & Schmidt, R. M. 1987, J. Geophys. Res., 92, 6350
Holsapple, K. A. 1993, Annu. Rev. Earth Planet. Sci., 21, 333
Holsapple, K. A. 2001, Icarus, 154, 432
Itagaki, Y., Tamura, H., Watanabe, Y., et al. 2019, Int. J. Impact Eng., 123, 38
Ivanov, B. A. 2001, Space Sci. Rev., 96, 87
Ivanov, B. A., Melosh, H. J., Pierazzo, E. 2010, Special paper of the geological society of America, 465, 29
Krishna, N. & Kumar, P. S. 2016, Icarus, 264, 274
Krüger, T., Hergarten, S., & Kenkmann, T. 2018, J. Geophys. Res.: Planets, 123, 2667
Kurosawa, K., Okamoto, T., & Genda, H. 2018, Icarus, 301, 219
Li, H., Yue, Z., & Zhang, N. 2025, Icarus, 435, 116579
Liu, T., Luther, R., Manske, L., et al. 2022, J. Geophys. Res.: Planets, 127, 8, e2022JE007264
Luo, F., Xiao, Z., Xu, R., et al. 2025, Commun. Earth Environ., 6, 284
Ma, P., Xiao, Z., Wang, Y., et al. 2025, Planet. Sci. J., 6, 151
Manske, L., Marchi, S., Plesa, A.-C., et al. 2021, Icarus, 357, 114128
Marchi, S., Mottola, S., Cremonese, G., et al. 2009, AJ, 137, 4936
Martellato, E., Vivaldi, V., Massironi, M., et al. 2017, Meteor. Planet. Sci., 52, 1388
Maxwell, D. E. 1977, Impact and Explosion Cratering: Planetary and Terrestrial Implications, 1003
Melosh, H. J. 1989, Impact cratering: A geologic process, 29517
Michel, P., Benz, W., Tanga, P., et al. 2001, Science, 294, 1696
Naidu, S. P., Benner, L. A. M., Brozovic, M., et al. 2020, Icarus, 348, 113777
Nakazawa, S., Watanabe, S., Iijima, Y., et al. 2002, Icarus, 156, 539
Neukum, G., Koenig, B., & Arkani-Hamed, J. 1975, Moon, 12, 201
Neukum, G., Ivanov, B. A., & Hartmann, W. K. 2001, Space Sci. Rev., 96, 55
Oberbeck, V. R. & Quaide, W. L. 1968, Icarus, 9, 446
Oberbeck, V. R. 1971, J. Geophys. Res., 76, 5732
Okeefe, J. D. & Ahrens, T. J. 1977, in Lunar Planet. Sci. Conf., 3, 3357
Ohnaka, M. 1995, Geophys. Res. Lett., 22, 25
'Oumuamua ISSI Team, Bannister, M. T., Bhandare, A., et al. 2019, Nat. Astron., 3, 594
Owen, J. M., DeCoster, M. E., Graninger, D. M., et al. 2022, Planet. Sci. J., 3, 218
Pierazzo, E., Artemieva, N., Asphaug, E., et al. 2008, Meteor. Planet. Sci., 43, 1917
Pike, R. J. 1974, Geophys. Res. Lett., 1, 291
Pike, R. J. 1977, Impact and Explosion Cratering: Planetary and Terrestrial Implications, 489
Pike, R. J. 1980, in Lunar Planet. Sci. Conf., 3, 2159
Plescia, J. B. & Cintala, M. J. 2012, J. Geophys. Res.: Planets, 117, E00H12
Potter, R. W. K. & Collins, G. S. 2013, Meteor. Planet. Sci., 48, 744
Raducan, S. D., Davison, T. M., & Collins, G. S. 2020, Planet. Space Sci., 180, 104756
Raducan, S. D., Jutzi, M., Davison, T. M., et al. 2022, Int. J. Impact Eng., 162, 104147
Rajšić, A., Miljković, K., Wójcicka, N., et al. 2021, Earth Space Sci., 8, e2021EA001887
Scheeres, D. J., Hartzell, C. M., Sánchez, P., et al. 2010, Icarus, 210, 968
Scheeres, D. J., Britt, D., Carry, B., et al. 2015, Asteroids IV, 745
Schmidt, R. M. & Housen, K. R. 1987, Int. J. Impact Eng., 5, 543
Schultz, P. H. & Gault, D. E. 1985, J. Geophys. Res., 90, 3701
Shoemaker, E. M. 1960, Ph.D. Thesis, Princeton University, New Jersey
Shuvalov, V. V. 2020, Solar Sys. Res., 54, 167
Stickle, A. M., DeCoster, M. E., Burger, C., et al. 2022, Planet. Sci. J., 3, 248
Stopar, J. D., Hawke, B. R., Robinson, M. S., et al. 2014, Icarus, 243, 337
Stopar, J. D., Robinson, M. S., Barnouin, O. S., et al. 2017, Icarus, 298, 34
Sugiura, K., Kobayashi, H., & Inutsuka, S. 2018, A&A, 620, A167
Susorney, H. C. M., Barnouin, O. S., Stickle, A. M. 2017, in Proceedings of the Hypervelocity Impact Symposium, 14, 421
Tatsumi, E. & Sugita, S. 2018, Icarus, 300, 227
Tillotson, J. H. 1962, General Atomic Report GA-3216. 1962. Technical Report, 3216
Wang, Y., Xiao, Z., Ma, P., et al. 2024, J. Earth Sci., 35, 708
Werner, S. C., Harris, A. W., & Neukum, G., et al. 2002, Icarus, 156, 287
Wilcox, B. B., Robinson, M. S., Thomas, P. C., et al. 2005, Meteor. Planet. Sci., 40, 695
Wu, B., Wang, Y., Werner, S. C., et al. 2022, Geophys. Res. Lett., 49, e2022GL100886
Wu, S., Chi, R., Zhang, H., et al. 2026, Adv. Space Res., 77, 2676
Wünnemann, K., Collins, G. S., & Melosh, H. J. 2006, Icarus, 180, 514
Wünnemann, K., Collins, G. S., & Osinski, G. R. 2008, Earth Planet. Sci. Lett., 269, 530
Wünnemann, K., Nowka, D., Collins, G. S. 2011, in Proceedings of the Hypervelocity Impact Symposium, 20, 1
Xiao, Z. 2016, J. Geophys. Res.: Planets, 121, 2404
Xie, M., Xiao, Z., Zhang, X., et al. 2020, J. Geophys. Res.: Planets, 125, e2019JE006112
Xie, M., Xiao, Z., Xu, L., et al. 2021, Nat. Astron., 5, 128
Xu, R., Xiao, Z., Luo, F., et al. 2023, Nat. Commun., 14, 1173
Xu, R., Xiao, Z., Wang, Y., et al. 2024, Commun. Earth Environ., 5, 641
Zhang, Y., Michel, P., Richardson, D. C., et al. 2021, Icarus, 362, 114433

Appendix A: Supporting material

Text A.1. Resolution test and mesh geometries of iSALE-2D simulations

We carried out sensitivity tests for the grid resolution (Fig. A.1), revealing that a resolution of 15 cells per projectile radius (CPPR) for spherical impactor (i.e., 1 cell = 1/15 equivalent radius) provides the best compromise between reasonable computation time and sufficient accuracy. It is notable that for oblate impactors, CPPR was defined as the number of grid cells per the impactor's short radius (Fig. A.2; Table A.1). Resolution tests reveal that actual grid sizes of oblate impactors smaller than those applied for spherical impactors (e.g., for impactors with AR = 10:1 and CPPR = 5, 1 cell = 1/23 equivalent spherical radius) ensure that the crater morphometric differences induced by grid resolution are less than ~1% (Fig. A.2).

We set high-resolution zone for the computational grid of the impact area, which had dimension of two times of the final crater diameter and depth. This zone was surrounded by a zone of progressively lower resolution, where the cell increased by a factor of 1.03 from the previous cell, in order to avoid spurious shock wave reflections at the target boundaries. Detailed mesh geometries of all models are listed in Table A.1.

Text A.2. Material strength models of iSALE-2D simulations

In DRPR model, the yield strength (Y) is defined as a linear function of overburden lithostatic pressure (P): $Y = \min(Y_0 + f \times P, Y_{Lim})$, where Y_0 is the cohesion, f is the friction coefficient, and Y_{Lim} is the high-pressure limiting strength. We set $Y_0 = 0.01$ MPa and $f = 0.6$ for all models which is suitable for lunar crustal materials (e.g., Martellato et al. 2017; Li et al. 2025).

The ROCK model defines the yield strength as $Y = Y_{d0} \times D_s + Y_{t0} \times (1\text{-}D_s)$, where Y_{t0} and Y_{d0} are the cohesions of intact and fully damaged material, respectively, and D_s is a scalar measure of damage (0 = intact; 1 = damaged; Ivanov et al. 2010). We set $Y_{t0} = 31.9$ MPa and $Y_{d0} = 0.1$ MPa for high-strength monolithic impactors, which is typical for lunar impact simulations (e.g., Martellato et al. 2017; Liu et al. 2022).

For rubble-pile asteroids, its cohesive strength and internal structure are not well understood (e.g., Stickle et al. 2022). Therefore, we carried out the sensitive test for final crater morphometries to different combinations of impactor strength models (i.e., DRPR vs. ROCK), intact cohesion of 1 to 10 kPa, and damaged cohesion of 0.1 to 10 kPa, following previous studies on rubble-pile asteroids (e.g., Raducan et al. 2020; Zhang et al. 2021; Raducan et al. 2022; Stickle et al. 2022). Fig. A.3 shows the sensitive test results of different rubble-pile impactor models, indicating that the selections of strength models and relatively low cohesive strength (~1 kPa) of impactors have negligible effect on crater morphometries.

Text A.3. Resolution test and estimations of impact melt volume

The total melt production is the sum of all tracer masses with peak shock pressures exceeding 60 GPa (Manske et al. 2021; Liu et al. 2022). Due to the required high shock pressure for vaporization (e.g., >100 GPa for basalts), vapor mass is neglectable compared to the mass of the molten material for the impact velocity on the Moon (Okeefe & Ahrens 1977; Manske et al. 2021; Liu et al. 2022). Therefore, we do not distinguish between melting and vaporization and denote both with "impact-induced melt" (e.g., Liu et al. 2022). The impact melt volume (V_m) is calculated by dividing the total melt mass by the initial density of the tracer material. In addition, the modelled melt volume is affected by resolution, with higher resolution producing larger and more accurate melt estimates (Wünnemann et al. 2008). Therefore, we conducted related resolution test (Fig. A.4), revealing that when the CPPR exceeded 80, the numerical error on the melt volume was <3%. Accordingly, we employed 80–120 CPPR for all models to determine the impact melt volume (detailed mesh geometries are listed in Table A.3).

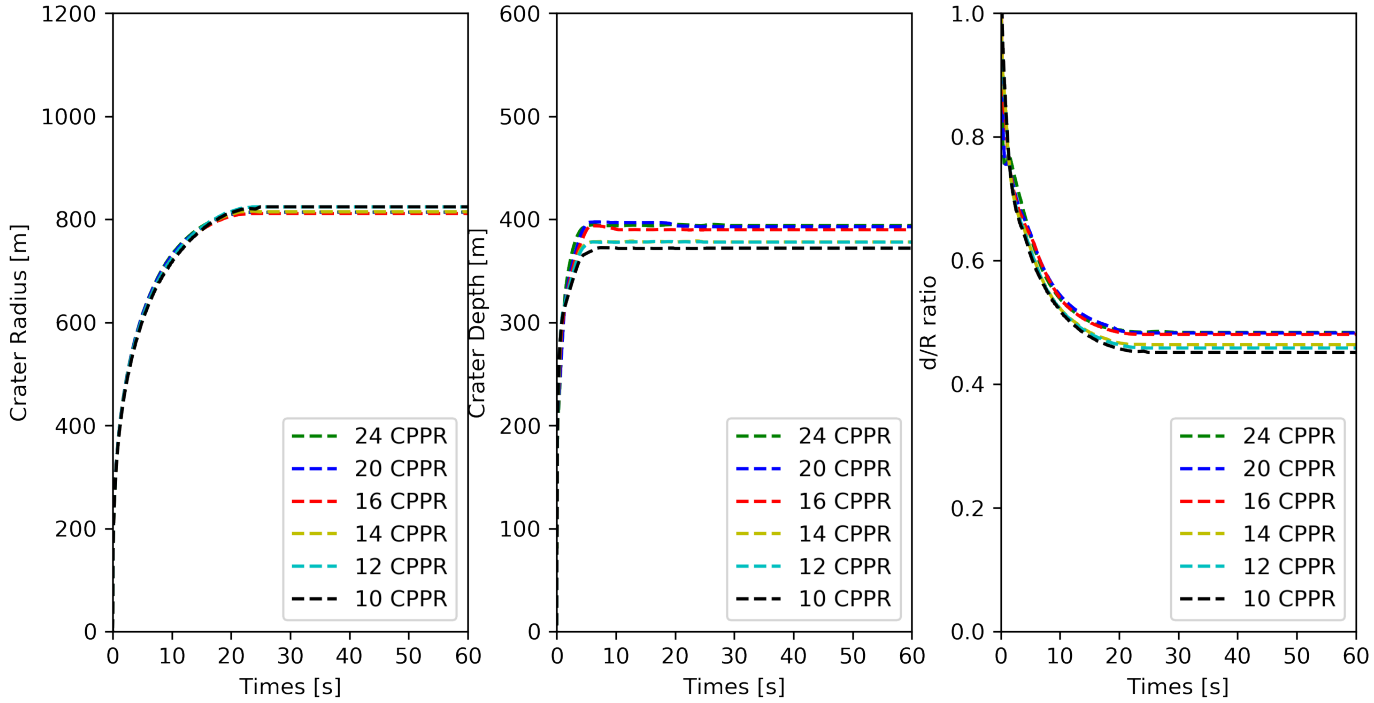

Fig. A.1: Resolution test of iSALE-2D simulation. Crater radius (left), crater depth (middle), and depth-to-radius ratio (right) as a function of time for an impact at resolutions between 10 and 24 CPPR (i.e., cells per projectile radius). The crater radius and depth are measured at the pre-impact surface.

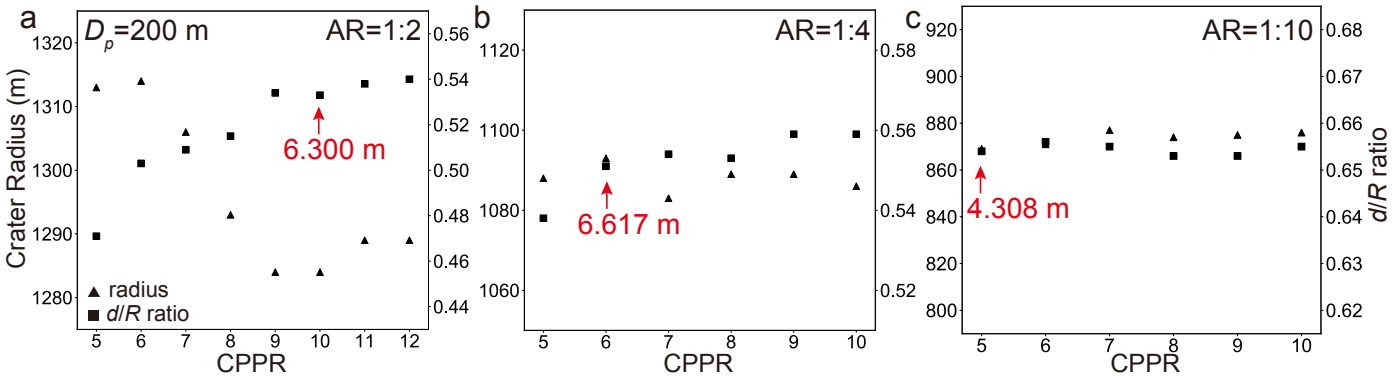

Fig. A.2: Resolution test for oblate impactors with an equivalent spherical diameter D_p = 200 m and aspect ratios (AR) of 1:2 (a), 1:4 (b), and 1:10 (c). CPPR of oblate impactor was defined as the number of grid cells per short radius of the impactor. As CPPR increases and the effective grid size of oblate impactors becomes smaller than that applied for spherical impactors (i.e., 6.67 m for D_p = 200 m and CPPR = 15; Fig. A.1), crater morphometric parameters converge with variations of <~1%. Red arrows indicate the adopted grid resolutions for oblate impactors, corresponding to CPPR values of 10, 6, and 5 for AR = 1:2 (2:1), 1:4 (4:1), and 1:10 (10:1), respectively. Detailed mesh geometries of all models are listed in Table A.1.

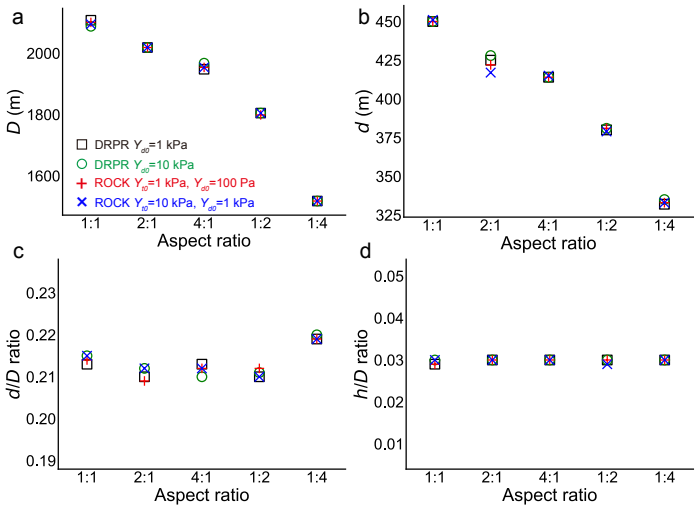

Fig. A.3: Selections of strength models and cohesive strength of impactors have negligible effect on crater morphometries: (a) crater diameter; (b) depth; (c) depth-to-diameter ratio; (d) rim-height to diameter ratio. The cohesive strength of the impactor material was modelled using DRPR and ROCK models, with intact material cohesion varies from 1 to 10 kPa and damaged material cohesion varies from 0.1 to 10 kPa (see legend). All impactors have the same equivalent diameter of 100 m, with aspect ratios ranging from 4:1 to 1:4.

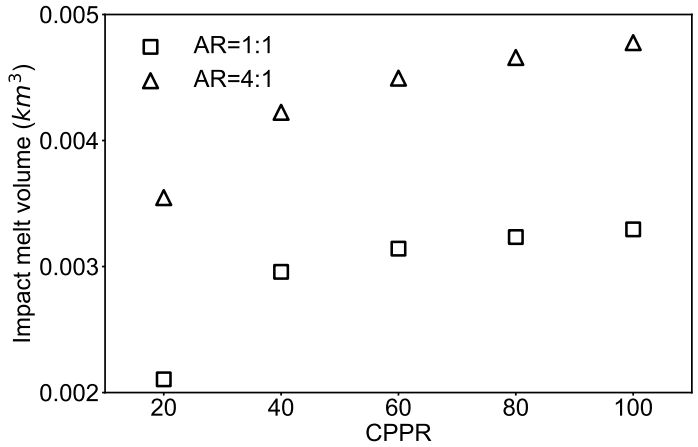

Fig. A.4: Resolution test of impact melt volume estimation. Impact melt volume as a function of model resolution (i.e., CPPR).

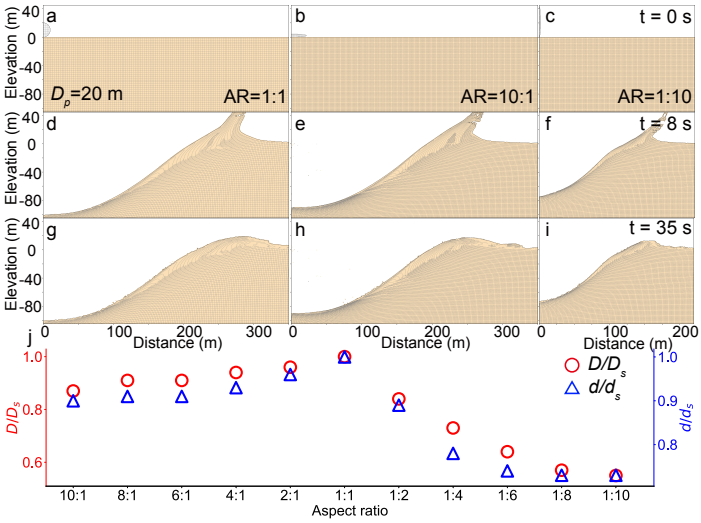

Fig. A.5: Same as Fig. 1 but for D_p = 20 m with AR = 10:1 and 1:10.

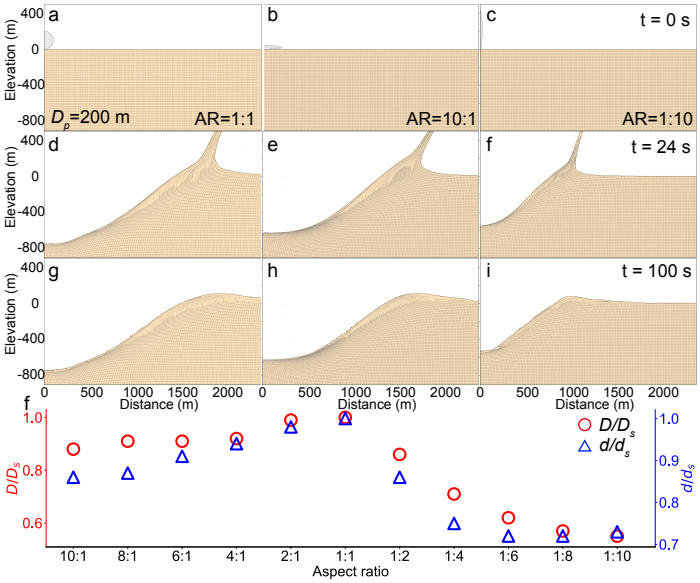

Fig. A.6: Same as Fig. 1 but for D_p = 200 m with AR = 10:1 and 1:10.

Table A.1: Description of projectile shapes and mesh geometry of oblate impact models.

D_p (m)	AR	Radius (m) a:b	Footprint (m^2)	GRID (m)	CPPRV	CPPRH	GRIDH			GRIDV		
	1:1	10 : 10	314	0.667	–	15	0	525	100	120	420	20
	2:1	12.6 : 6.3	499	0.63	10	20	0	555	100	120	445	20
	4:1	15.87 : 3.97	791	0.662	6	24	0	530	100	120	425	20
	6:1	18.17 : 3.028	1037	0.6056	5	30	0	580	100	120	465	20
	8:1	20 : 2.5	1257	0.5	5	40	0	700	100	120	560	20
20	10:1	21.54 : 2.154	1458	0.4308	5	50	0	815	100	120	650	20
	1:2	6.3 : 12.6	125	0.63	20	6	0	476	60	80	238	20
	1:4	3.97 : 15.87	50	0.662	24	5	0	423	60	80	227	20
	1:6	3.028 : 18.17	29	0.6056	30	5	0	413	60	80	248	20
	1:8	2.5 : 20	20	0.5	40	5	0	480	60	80	300	20
	1:10	2.154 : 21.54	15	0.4308	50	5	0	534	60	80	348	20
	1:1	50 : 50	7854	3.33	–	15	0	480	80	100	360	20
	2:1	63 : 31.5	12469	3.15	10	20	0	510	80	100	381	20
	4:1	79.37 : 19.84	19791	3.307	6	24	0	485	80	100	363	20
	6:1	90.86 : 15.14	25936	3.028	5	30	0	530	80	100	396	20
	8:1	100 : 12.5	31416	2.5	5	40	0	640	80	100	480	20
100	10:1	107.7 : 10.77	36440	2.154	5	50	0	743	80	100	557	20
	1:2	31.5 : 63	3117	3.15	20	10	0	510	80	100	381	20
	1:4	19.84 : 79.37	1237	3.307	24	6	0	485	80	100	363	20
	1:6	15.14 : 90.86	720	3.028	30	5	0	330	60	80	297	20
	1:8	12.5 : 100	491	2.5	40	5	0	400	60	80	360	20
	1:10	10.77 : 107.7	364	2.154	50	5	0	418	60	80	418	20
	1:1	100 : 100	31416	6.67	–	15	0	450	80	100	330	20
	2:1	126 : 63	49876	6.3	10	20	0	476	80	100	350	20
	4:1	158.7 : 39.7	79123	6.62	6	24	0	453	80	100	332	20
	6:1	181.7 : 30.28	103719	6.056	5	30	0	495	80	100	363	20
	8:1	200 : 25	125664	5	5	40	0	600	80	100	440	20
200	10:1	215.4 : 21.54	145761	4.308	5	50	0	696	80	100	511	20
	1:2	63 : 126	12469	6.3	20	10	0	476	80	100	350	20
	1:4	39.7 : 158.7	4951	6.62	24	6	0	453	80	100	332	20
	1:6	30.28 : 181.7	2880	6.056	30	5	0	495	80	100	363	20
	1:8	25 : 200	1963	5	40	5	0	600	80	100	440	20
	1:10	21.54 : 215.4	1458	4.308	50	5	0	696	80	100	511	20

Notes. CPPRV and CPPRH are cells per projectile radius (CPPR) in vertical and horizontal directions of the projectile, respectively. Footprint is the foot print areas of projectile.

Table A.2: Parameters used in the numerical simulations.

Description	**Projectile**	**Target**
Projectile diameter (m)	20, 100, 200	–
Projectile aspect ratio (AR)	1:1, 2:1, 4:1, 6:1, 8:1, 10:1, 1:2, 1:4, 1:6, 1:8, 1:10	
Gravitational acceleration (m s^{-2})	1.62	
Impact velocity (km s^{-1})	12.7	
Equation of state	Basalt Tillotson	
Thermal		
Solidus (at zero pressure) (K)	1360	
Thermal softening parameter	1.2	
Constant in Simon approximation (Pa)	4.5×10^{9}	
Exponent in Simon approximation	3.0	
Strength		
Poisson ratio	0.25	0.25
Coefficient of internal friction (intact rock) f_t	1.1	–
Cohesion (intact rock) Y_{t0}	31.9 MPa	–
Limiting strength at high pressure (intact rock)	2.47 GPa	–
Coefficient of internal friction (damaged) f_d	0.63	0.6
Cohesion (damaged) Y_{d0}	0.1 MPa, 1 kPa	0.01 MPa
Limiting strength at high pressure (damaged)	2.47 GPa	2.47 GPa
Damage		
Minimum failure strain for low pressure states	1×10^{-4}	
Increase in failure strain with pressure	1×10^{-11}	
Pressure above which failure is always compressional (Pa)	3×10^{8}	
Porosity		
Initial porosity	20%	
Elastic volumetric strain threshold	-1.88×10^{-4}	
Distension transition from exponential to power-law compaction	1.0	
Compaction rate in exponential compaction regime	0.9	
Ratio of porous to solid material sound speed at zero pressure	1.0	

Table A.3: Description of projectile shapes and mesh geometry of oblate impact models for impact melt volume estimation.

D_p (m)	AR	Radius (m) a:b	GRID (m)	CPPRV	CPPRH	GRIDH			GRIDV		
	1:1	10 : 10	0.125	–	80	0	640	60	80	1040	20
	2:1	12.6 : 6.3	0.126	50	100	0	640	60	80	1040	20
	4:1	15.87 : 3.97	0.1587	25	100	0	640	60	80	1040	20
	6:1	18.17 : 3.028	0.1514	20	120	0	640	60	80	1040	20
	8:1	20 : 2.5	0.1667	15	120	0	640	60	80	1040	20
20	10:1	21.54 : 2.154	0.1795	12	120	0	640	60	80	1040	20
	1:2	6.3 : 12.6	0.126	100	50	0	640	60	80	1040	20
	1:4	3.97 : 15.87	0.1587	100	25	0	640	60	80	1040	20
	1:6	3.028 : 18.17	0.1514	120	20	0	640	60	80	1040	20
	1:8	2.5 : 20	0.1667	120	15	0	640	60	80	1040	20
	1:10	2.154 : 21.54	0.1795	120	12	0	640	60	80	1040	20
	1:1	50 : 50	0.625	–	80	0	640	60	80	1040	20
	2:1	63 : 31.5	0.63	50	100	0	640	60	80	1040	20
	4:1	79.37 : 19.84	0.7937	25	100	0	640	60	80	1040	20
	6:1	90.86 : 15.14	0.7572	20	120	0	640	60	80	1040	20
	8:1	100 : 12.5	0.8333	15	120	0	640	60	80	1040	20
100	10:1	107.7 : 10.77	0.8975	12	120	0	640	60	80	1040	20
	1:2	31.5 : 63	0.63	100	50	0	640	60	80	1040	20
	1:4	19.84 : 79.37	0.7937	100	25	0	640	60	80	1040	20
	1:6	15.14 : 90.86	0.7572	120	20	0	640	60	80	1040	20
	1:8	12.5 : 100	0.8333	120	15	0	640	60	80	1040	20
	1:10	10.77 : 107.7	0.8975	120	12	0	640	60	80	1040	20
	1:1	100 : 100	1.25	–	80	0	640	60	80	1040	20
	2:1	126 : 63	1.26	50	100	0	640	60	80	1040	20
	4:1	158.7 : 39.7	1.587	25	100	0	640	60	80	1040	20
	6:1	181.7 : 30.28	1.514	20	120	0	640	60	80	1040	20
	8:1	200 : 25	1.667	15	120	0	640	60	80	1040	20
200	10:1	215.4 : 21.54	1.795	12	120	0	640	60	80	1040	20
	1:2	63 : 126	1.26	100	50	0	640	60	80	1040	20
	1:4	39.7 : 158.7	1.587	100	25	0	640	60	80	1040	20
	1:6	30.28 : 181.7	1.514	120	20	0	640	60	80	1040	20
	1:8	25 : 200	1.667	120	15	0	640	60	80	1040	20
	1:10	21.54 : 215.4	1.795	120	12	0	640	60	80	1040	20

Notes. CPPRV and CPPRH are cells per projectile radius (CPPR) in vertical and horizontal directions of the projectile, respectively.

Table A.4: Morphometric parameters and cratering efficiency (π_v) of all modelled final craters and transient craters in this study.

D_p (m)	AR	D (m)	d (m)	d/D	h (m)	h/D	D_t (m)	d_t (m)	V_t (m^3)	π_v
20	1:1	570	120	0.211	19	0.033	434	101	6.69×10^6	1597
	2:1	549	115	0.209	18	0.033	417	98	6.12×10^6	1461
	4:1	533	111	0.208	17	0.032	402	95	5.62×10^6	1342
	6:1	520	109	0.210	17	0.033	396	92	5.39×10^6	1287
	8:1	516	109	0.211	17	0.033	393	92	5.29×10^6	1263
	10:1	495	108	0.218	17	0.034	391	91	5.19×10^6	1239
	1:2	477	107	0.224	17	0.035	359	94	4.22×10^6	1007
	1:4	415	94	0.227	15	0.035	315	82	2.46×10^6	587
	1:6	366	89	0.243	17	0.037	285	80	1.81×10^6	432
	1:8	327	88	0.268	13	0.039	260	77	1.53×10^6	365
	1:10	315	87	0.275	13	0.041	242	75	1.32×10^6	315
100	1:1	2208	473	0.214	62	0.028	1678	418	3.94×10^8	752
	2:1	2114	444	0.210	59	0.028	1613	392	3.61×10^8	689
	4:1	2047	438	0.214	58	0.028	1568	392	3.33×10^8	636
	6:1	2033	412	0.203	59	0.029	1544	347	3.21×10^8	613
	8:1	2014	407	0.202	59	0.029	1535	354	3.16×10^8	604
	10:1	1928	413	0.214	60	0.031	1512	354	3.11×10^8	594
	1:2	1925	399	0.207	53	0.028	1449	348	2.40×10^8	458
	1:4	1604	351	0.219	46	0.029	1224	313	1.44×10^8	275
	1:6	1408	340	0.241	45	0.032	1090	298	1.09×10^8	208
	1:8	1293	332	0.257	43	0.033	1005	301	0.92×10^8	176
	1:10	1191	338	0.284	43	0.036	922	307	0.80×10^8	153
200	1:1	3943	847	0.215	105	0.027	3002	750	2.26×10^9	540
	2:1	3900	831	0.213	101	0.026	2885	752	2.08×10^9	497
	4:1	3634	794	0.218	104	0.028	2767	712	1.91×10^9	456
	6:1	3603	773	0.215	102	0.028	2749	675	1.84×10^9	439
	8:1	3575	740	0.207	103	0.029	2730	623	1.82×10^9	435
	10:1	3528	731	0.207	106	0.030	2705	625	1.79×10^9	427
	1:2	3396	732	0.216	93	0.027	2570	659	1.38×10^9	329
	1:4	2814	632	0.224	78	0.028	2185	579	0.84×10^9	201
	1:6	2441	609	0.250	76	0.031	1914	554	0.62×10^9	148
	1:8	2245	612	0.273	77	0.034	1730	543	0.52×10^9	124
	1:10	2046	619	0.302	78	0.038	1577	545	0.45×10^9	107

Table A.5: Original and normalized maximum excavation depth (d_{exc_max}), median excavation depth (d_{exc_med}), impact melt fraction of rim materials ($Melt_R\%$), and total impact melt volume (V_m) for all models in this study.

D_p (m)	AR	d_{exc_max} (m)	d_{exc_max}/d	d_{exc_max}/d_t	d_{exc_med} (m)	$Melt_R\%$	V_m (km^3)
20	1:1	45	0.38	0.45	20	0.7%	2.59×10^{-5}
	2:1	44	0.38	0.45	20	0.9%	3.53×10^{-5}
	4:1	43	0.39	0.45	20	1.1%	3.82×10^{-5}
	6:1	42	0.39	0.46	20	1.1%	4.00×10^{-5}
	8:1	43	0.39	0.47	19	1.2%	4.08×10^{-5}
	10:1	43	0.40	0.47	19	1.2%	4.16×10^{-5}
	1:2	40	0.37	0.43	15	0.3%	0.60×10^{-5}
	1:4	36	0.38	0.44	12	0.3%	0.15×10^{-5}
	1:6	35	0.39	0.44	10	0.2%	0.07×10^{-5}
	1:8	35	0.40	0.45	10	0.2%	0.04×10^{-5}
	1:10	36	0.41	0.48	10	0.3%	0.03×10^{-5}
100	1:1	182	0.39	0.44	82	1.4%	3.24×10^{-3}
	2:1	175	0.39	0.45	77	1.8%	4.41×10^{-3}
	4:1	174	0.40	0.45	74	1.8%	4.77×10^{-3}
	6:1	171	0.42	0.49	74	2.0%	5.00×10^{-3}
	8:1	171	0.42	0.48	71	1.8%	5.10×10^{-3}
	10:1	171	0.41	0.48	72	2.2%	5.20×10^{-3}
	1:2	159	0.40	0.46	58	0.7%	0.75×10^{-3}
	1:4	147	0.42	0.47	48	0.5%	0.19×10^{-3}
	1:6	148	0.43	0.50	44	0.4%	0.09×10^{-3}
	1:8	151	0.45	0.50	44	0.5%	0.05×10^{-3}
	1:10	156	0.46	0.51	48	0.4%	0.04×10^{-3}
200	1:1	324	0.38	0.43	137	1.6%	2.59×10^{-2}
	2:1	312	0.38	0.42	135	2.1%	3.53×10^{-2}
	4:1	308	0.39	0.43	129	2.0%	3.82×10^{-2}
	6:1	306	0.40	0.45	130	2.4%	4.00×10^{-2}
	8:1	307	0.41	0.49	118	2.0%	4.08×10^{-2}
	10:1	304	0.42	0.49	123	2.5%	4.16×10^{-2}
	1:2	287	0.39	0.43	104	0.8%	0.60×10^{-2}
	1:4	268	0.42	0.46	83	0.7%	0.15×10^{-2}
	1:6	276	0.45	0.50	82	0.5%	0.07×10^{-2}
	1:8	283	0.46	0.52	93	0.6%	0.04×10^{-2}
	1:10	286	0.46	0.52	93	0.3%	0.03×10^{-2}

Table A.6: Morphometric parameters and cratering efficiency (π_v) of all modelled final craters and transient craters of rubble-pile asteroid impacts with different strength models.

Models	AR	D (m)	d (m)	d/D	h (m)	h/D	D_t (m)	d_t (m)	V_t (m^3)	π_v
DRPR Y_{d0}=1 kPa	1:1	2108	450	0.213	61	0.029	1599	398	3.33×10^8	795
	2:1	2019	425	0.210	61	0.030	1529	365	3.05×10^8	728
	4:1	1948	414	0.213	59	0.030	1490	394	2.81×10^8	671
	1:2	1805	380	0.210	54	0.030	1363	327	2.03×10^8	485
	1:4	1518	332	0.219	45	0.030	1164	292	1.22×10^8	291
DRPR Y_{d0}=10 kPa	1:1	2088	450	0.215	62	0.030	1602	398	3.35×10^8	800
	2:1	2019	428	0.212	62	0.030	1529	364	3.05×10^8	728
	4:1	1968	414	0.210	58	0.030	1491	392	2.81×10^8	671
	1:2	1805	381	0.211	54	0.030	1364	330	2.05×10^8	489
	1:4	1518	335	0.220	45	0.030	1164	293	1.22×10^8	291
ROCK Y_{d0}=1 kPa Y_{d0}=100 Pa	1:1	2101	450	0.214	61	0.029	1599	399	3.33×10^8	795
	2:1	2019	422	0.209	61	0.030	1530	364	3.05×10^8	728
	4:1	1954	414	0.212	58	0.030	1491	394	2.81×10^8	671
	1:2	1799	381	0.212	54	0.030	1363	329	2.04×10^8	487
	1:4	1518	333	0.219	45	0.030	1164	293	1.22×10^8	291
ROCK Y_{d0}=10 kPa Y_{d0}=1 kPa	1:1	2095	451	0.215	62	0.030	1600	398	3.33×10^8	795
	2:1	2019	427	0.212	61	0.030	1528	365	3.05×10^8	728
	4:1	1954	415	0.212	59	0.030	1491	395	2.81×10^8	671
	1:2	1805	379	0.210	52	0.029	1362	326	2.03×10^8	485
	1:4	1518	333	0.219	45	0.030	1165	292	1.23×10^8	294

Notes. The equivalent diameter (D_p) of all impactors is 100 m.